AGU PUBLICATIONS

Water Resources Research

RESEARCH ARTICLE

10.1002/2015WR017019

Key Points:
- Steady state analytical solutions for pumping in a rectangular aquifer are developed
- The conformal mapping method together with the complex variable techniques is applied
- The conformal mapping method outperforms the direct image-well method

Correspondence to:
C. Lu,
chunhui.lu@monash.edu

Citation:
Lu, C., P. Xin, L. Li, and J. Luo (2015), Steady state analytical solutions for pumping in a fully bounded rectangular aquifer, *Water Resour. Res.*, *51*, 8294–8302, doi:10.1002/2015WR017019.

Received 2 FEB 2015
Accepted 10 SEP 2015
Accepted article online 15 SEP 2015
Published online 20 OCT 2015

Steady state analytical solutions for pumping in a fully bounded rectangular aquifer

Chunhui Lu[1,2], Pei Xin[1], Ling Li[1,3], and Jian Luo[4]

[1]State Key Laboratory of Hydrology-Water Resources and Hydraulic Engineering, Hohai University, Nanjing, China, [2]Monash Water for Liveability, Civil Engineering Department, Monash University, Clayton, Victoria, Australia, [3]School of Civil Engineering, University of Queensland, Brisbane, Queensland, Australia, [4]School of Civil and Environmental Engineering, Georgia Institute of Technology, Atlanta, Georgia, USA

Abstract Using the Schwartz-Christoffel conformal mapping method together with the complex variable techniques, we derive steady state analytical solutions for pumping in a rectangular aquifer with four different combinations of impermeable and constant-head boundaries. These four scenarios include: (1) one constant-head boundary and three impermeable boundaries, (2) two pairs of orthogonal impermeable and constant-head boundaries, (3) three constant-head boundaries and one impermeable boundary, and (4) four constant-head boundaries. For these scenarios, the impermeable and constant-head boundaries can be combined after applying the mapping functions, and hence only three image wells exist in the transformed plane, despite an infinite number of image wells in the real plane. The closed-form solutions reflect the advantage of the conformal mapping method, though the method is applicable for the aspect ratio of the rectangle between 1/10.9 and 10.9/1 due to the limitation in the numerical computation of the conformal transformation from a half plane onto an elongated region (i.e., so-called **"**crowding**"** phenomenon). By contrast, for an additional scenario with two parallel constant-head boundaries and two parallel impermeable boundaries, an infinite series of image wells is necessary to express the solution, since it is impossible to combine these two kinds of boundaries through the conformal transformation. The usefulness of the results derived is demonstrated by an application to pumping in a finite coastal aquifer.

1. Introduction

Analytical mathematical models used to tackle pumping-induced flow problems are mostly based on the assumption that the aquifer is of infinite areal extent [e.g., *Lu et al*., 2009; *Weber and Chapuis*, 2013]. This assumption is only valid if the zone of influence boundary of a pumping well does not reach to the nearby impermeable (i.e., no-flow) boundaries (such as bedrocks, glacial tills, fault blocks, or relatively impervious rock) and surface water bodies (i.e., constant-head boundaries, such as streams, rivers, lakes, canals, and seas) during the extraction or injection period. However, if it interfaces with one or more of these influence boundaries, the assumption of an infinite domain no longer holds and the influence from boundary conditions must be taken into account [*Ferris et al*., 1962].

The impact of boundary conditions on pumping has long been recognized in previous studies of both noncoastal and coastal aquifers [e.g., *Chan*, 1976; *Latinopoulos*, 1982; *Corapcioglu et al*., 1983; *Zhan*, 1999; *Intaraprasong and Zhan*, 2007; *Lu et al*., 2012; *Lu and Luo*, 2014]. *Wilson* [1993] explored pumping from a noncoastal aquifer bounded by a stream and a barrier and by two parallel streams, respectively. The author adopted the Schwartz-Christoffel conformal mapping method to derive the analytical solutions for the two scenarios. Well pumping in a fully bounded rectangular coastal aquifer with three impermeable boundaries and one constant boundary (i.e., coastal boundary) was previously explored by *Mantoglou* [2003] using the image-well method. For a fully bounded coastal aquifer, theoretically, there exists an infinity of reflection image wells. However, the author expressed equations in a truncated summation series, while a closed-form solution was not given, despite its usefulness for pumping in an aquifer where more reflection image wells are needed to ensure an accurate solution.

Recently, *Lu and Luo* [2014] explored pumping in a rectangular coastal aquifer bounded by two parallel impermeable boundaries and two parallel constant-head boundaries (i.e., a head-controlled coastal system).

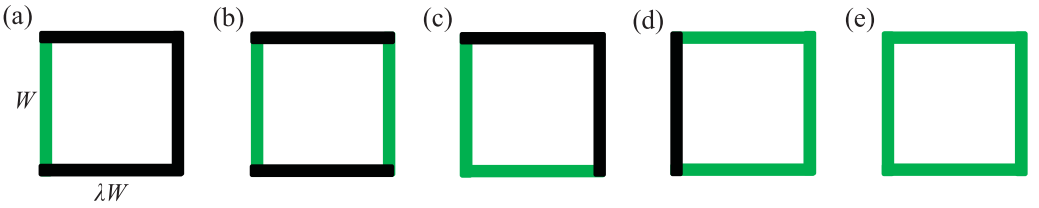

Figure 1. Schematic diagram of a rectangular aquifer bounded, respectively, by (a) one constant-head boundary (in green) and three impermeable boundaries (in black), (b) two parallel constant-head boundaries and two parallel impermeable boundaries, (c) two pairs of orthogonal impermeable and constant-head boundaries, (d) one impermeable boundary and three constant-head boundaries, and (e) four constant-head boundaries.

They expressed the solution in the series form that superposes infinite image wells. Importantly, they found a linear relationship between the domain width and length, under which the effects from lateral and horizontal boundaries on the interface toe location and maximum pumping rate are counteracted. The derived results could offer guidance for designing domain size and well locations to minimize the effects from boundaries in numerical simulations and laboratory experiments.

In this study, we derive steady state analytical solutions for pumping in a fully bounded rectangular aquifer relying on the Schwartz-Christoffel conformal mapping method. The main advantage of using the conformal mapping method, as will be shown, is that it can transform the boundary conditions into much simpler scenarios, which can facilitate the derivation of analytical solutions. We consider five boundary condition scenarios with different combinations of impermeable and constant-head boundaries. The usefulness of derived solutions will be demonstrated by an application to pumping in a bounded rectangular confined coastal aquifer.

2. Method

2.1. Boundary Condition Scenarios

We consider a pumping well located in a homogeneous, rectangular aquifer bounded by five scenarios, as shown in Figure 1. Scenario 1 (labeled as "S1"; Figure 1a) includes three impermeable boundaries and one constant-head boundary, which is the same aquifer type as that studied by *Mantoglou* [2003]. S2 considers two parallel impermeable boundaries and two parallel constant-head boundaries (Figure 1b), which is the aquifer type investigated by *Lu and Luo* [2014]. Two pairs of orthogonal impermeable and constant-head boundaries are assumed in S3 (Figure 1c). S4 (Figure 1d), and S5 (Figure 1e) assume that the aquifer is bounded by one impermeable boundary and three constant-head boundaries, and four constant-head boundaries, respectively. In addition to these scenarios, an aquifer bounded by four impermeable boundaries has been studied by *Chan* [1976]. This scenario was not considered in this study since a steady state condition never occurs.

Flow systems are assumed at steady state conditions. Surface recharge and regional flow are neglected for simplicity, and they can be readily added once the solutions are derived. We further assume that x and y axes are aligned with the lower and left boundaries, respectively, with the origin at the intersection of these two boundaries (Figure 2). The well is at an arbitrary location with coordinates of (x_w, y_w) and with a constant pumping rate of Q_w [L^3/T]. The domain length (in the x axis direction) and width (in the y axis direction) are λW [L] and W [L], respectively, where λ is the aspect ratio.

The discharge potential is employed to express pumping and confined flow, and the relation between potential and head is given as [*Strack*, 1989]:

$$\Phi = KHh = \frac{Q_w}{2\pi} \ln\left[\frac{\sqrt{(x-x_w)^2+(y-y_w)^2}}{r_0}\right] + h_0 \tag{1}$$

in which K[L/T] is the hydraulic conductivity, h[L] and h_0[L] are the piezometric head at (x, y) and at the distance of r_0 from the well. Therefore, once the solution of Φ is derived, the piezometric head is obtained.

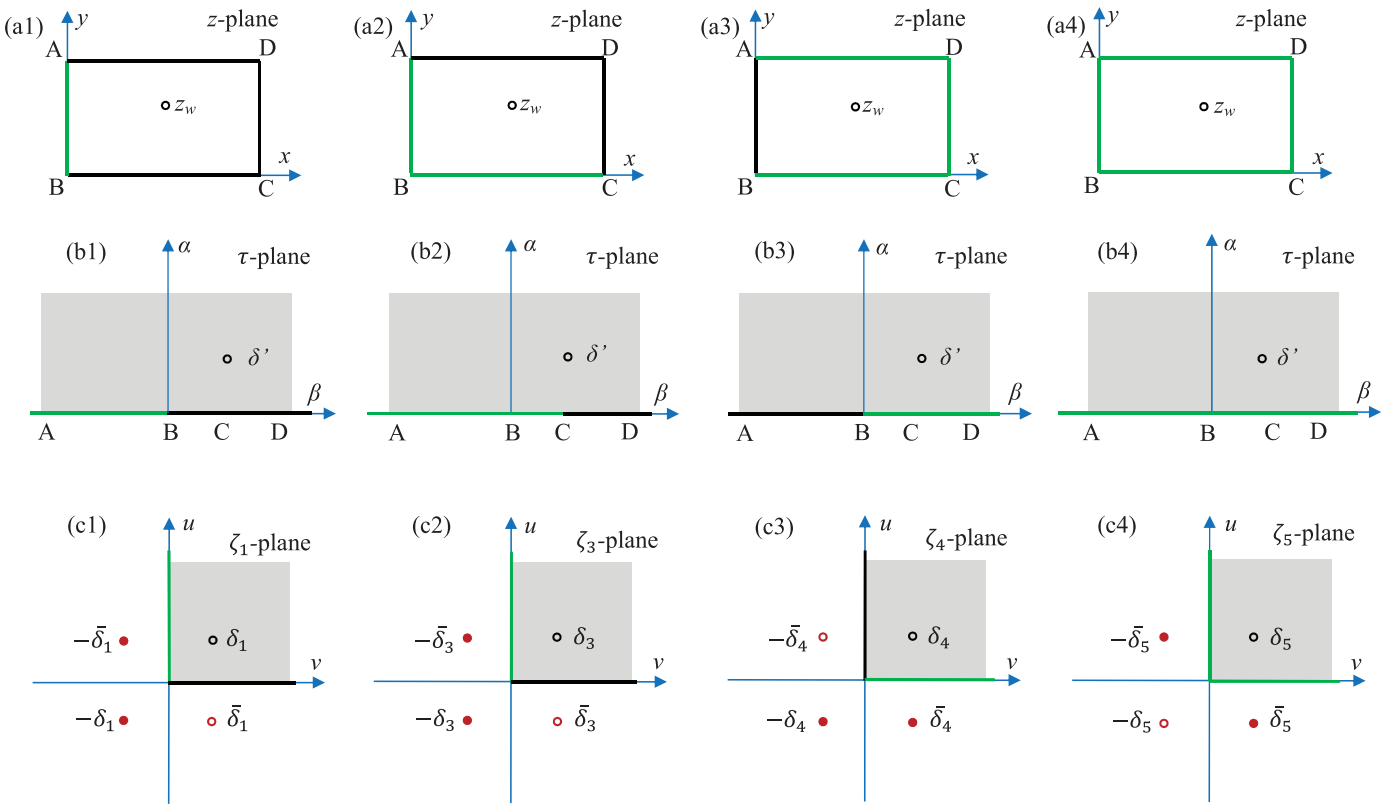

Figure 2. Conformal mapping for four scenarios: (a1)–(c1) S1, (a2)–(c2) S3, (a3)–(c3) S4, and (a4)–(b4) S5. Boundaries in green and blue represent the constant-head and impermeable boundaries, respectively. Black hollow circles indicate the locations of the real well. The red hollow circles represent the image wells with the same type (i.e., injection/extraction) as the real well, while red solid circles denote the image wells with the opposite type as the real well.

2.2. Conformal Mapping Method and Analytical Derivation

The Schwartz-Christoffel conformal mapping method is used to derive the analytical solutions. An examination of these boundary condition scenarios indicates that S1 and S3–S5 can be categorized into the same type where the impermeable and constant-head boundaries can be combined after applying the mapping functions. By contrast, the impermeable and constant-head boundaries in S2 are unable to be combined with the application of conformal mapping, as they meet at the origin and infinity. As such, the solution of S2 must be expressed in a series form. In the following, we first derive analytical solutions for S1 and S3–S5, and then for S2.

For S1, a well is located in a rectangular domain bounded by one constant-head boundary and three impermeable boundaries. The vertices of the rectangular A–D in the z-plane are mapped onto the real axis of the τ-plane, as shown in Figures 2a1 and 2b1. The interior of the rectangular is then transformed to the upper half τ-plane. After transformation, the coordinates of points A–D in the τ-plane are: $\tau_A=-\infty$, $\tau_B=0$, $\tau_C=1$, and $\tau_D=1/m$. Therefore, the transformation follows the formula:

$$z(\tau)=C_1\int\frac{d\tau}{\sqrt{\tau(\tau-1)(\tau-1/m)}}+C_2 \tag{2}$$

in which C_1 and C_2 control the size of the rectangle and the location of the origin in the z-plane, respectively. $C_2=0$ because $z=0$ corresponds to $\tau=0$. To facilitate using the image-well method, the τ-plane is then transformed onto the ζ_1-plane through the transformation equation $\zeta_1=\tau^{1/2}$, as shown in Figure 2c1. This transformation leads to a simpler scenario, that is, well pumps in an upper right quarter plane bounded only by orthogonal impermeable and constant-head boundaries. As such, only three image wells exist in the solution [*Strack*, 1972, 1989].

Equation (2) can then be rewritten as:

$$z(\zeta_1)=C_3\int\frac{d\zeta_1}{\sqrt{(1-\zeta_1{}^2)(1-m\zeta_1{}^2)}} \tag{3}$$

in which $C_3=2C_1/\sqrt{m}$. Equation (3) is an incomplete elliptic integral of the first kind. m is determined based on the aspect ratio λ. The complete elliptic integrals with the upper limits equal to 1 and $1/\sqrt{m}$ are:

$$K(m)=\int_0^1\frac{d\zeta_1}{\sqrt{(1-\zeta_1{}^2)(1-m\zeta_1{}^2)}} \tag{4}$$

$$K(m)+iK(1-m)=\int_0^{1/\sqrt{m}}\frac{d\zeta_1}{\sqrt{(1-\zeta_1{}^2)(1-m\zeta_1{}^2)}} \tag{5}$$

The complete elliptic integrals for the distances between points B–C and between points B–D give:

$$\frac{K(m)}{K(1-m)}=\lambda \tag{6}$$

The proof of equation (6) can be found in Appendix A. Thus m can be easily found based on the value of λ. Note that the range of λ is limited between 1/10.9 and 10.9/1, due to the "crowding" phenomenon that occurs in the Schwartz-Christoffel transformation for elongated regions [*Howell and Trefethen*, 1990]. Once m is available, C_3 can be calculated by $\frac{\lambda W}{K(m)}$ (see Appendix A).

Applying the image-well method in the ζ_1-plane, the complex potential of S1 is expressed as [*Strack*, 1972, 1989]:

$$\Omega_1=\frac{Q_w}{2\pi}\ln\left[\frac{(\zeta_1-\delta_1)(\zeta_1-\overline{\delta_1})}{(\zeta_1+\delta_1)(\zeta_1+\overline{\delta_1})}\right]+\Phi_0 \tag{7}$$

in which Φ_0 is the value of the discharge potential along the constant-head boundary, δ_1 is the well location on the ζ_1-plane, and $\overline{\delta_1}$ represents the complex conjugate of δ_1.

We assume that $z/C_3=F(\zeta_1,m)$, where $F(\zeta_1,m)$ is the incomplete elliptic function of the first kind. One can find that [*Betz*, 1948]:

$$\zeta_1=sn(z/C_3)=\frac{sn(x/C_3)\overline{dn}(y/C_3)+icn(x/C_3)dn(x/C_3)\overline{sn}(y/C_3)\overline{cn}(y/C_3)}{\overline{cn}^2(y/C_3)+msn^2(x/C_3)\overline{sn}^2(y/C_3)}=Re^{i\theta} \tag{8}$$

in which *sn*, *cn*, and *dn* are the three standard forms of Jacobi elliptic integrals, which denote the *sine*, *cosine*, and *delta* amplitude elliptic functions, respectively; $\overline{sn}(y)$ stands for $sn(y,1-m)$, and similar definitions are made for $\overline{cn}(y)$ and $\overline{dn}(y)$. The values of *sn*, *cn*, and *dn* can be evaluated by *Matlab*® built-in functions. R and θ are expressed as $R^2=M_1^2+N_1^2$ and $\theta=\tan^{-1}(N_1/M_1)$, respectively, where M_1 and N_1 are the real and imaginary parts of ζ_1, respectively.

The complex potential for S1 is written by:

$$\Omega_1=\Phi_1+i\Psi_1 \tag{9}$$

in which Φ_1 and Ψ_1 are the flow potential and stream function for S1, respectively, and they can be expressed by four components: $\Phi_1=\Phi_1^1+\Phi_1^2+\Phi_1^3+\Phi_1^4+\Phi_0$ and $\Psi_1=\Psi_1^1+\Psi_1^2+\Psi_1^3+\Psi_1^4$, respectively. Similar definitions are made for S3–S5 by simply replacing the subscripts with 3–5, respectively. For S1, Φ_1^1-Φ_1^4 and Ψ_1^1-Ψ_1^4 are given as:

$$\Phi_1^1=\frac{Q_w}{4\pi}\ln\left[(M_1-M_{1w})^2+(N_1-N_{1w})^2\right] \tag{10}$$

$$\Phi_1^2=\frac{Q_w}{4\pi}\ln\left[(M_1-M_{1w})^2+(N_1+N_{1w})^2\right] \tag{11}$$

$$\Phi_1^3=-\frac{Q_w}{4\pi}\ln\left[(M_1+M_{1w})^2+(N_1+N_{1w})^2\right] \tag{12}$$

$$\Phi_1^4 = -\frac{Q_w}{4\pi}\ln\left[(M_1+M_{1w})^2+(N_1-N_{1w})^2\right] \tag{13}$$

$$\Psi_1^1 = \frac{Q_w}{2\pi}\tan^{-1}\left(\frac{N_1-N_{1w}}{M_1-M_{1w}}\right) \tag{14}$$

$$\Psi_1^2 = \frac{Q_w}{2\pi}\tan^{-1}\left(\frac{N_1+N_{1w}}{M_1-M_{1w}}\right) \tag{15}$$

$$\Psi_1^3 = -\frac{Q_w}{2\pi}\tan^{-1}\left(\frac{N_1+N_{1w}}{M_1+M_{1w}}\right) \tag{16}$$

$$\Psi_1^4 = -\frac{Q_w}{2\pi}\tan^{-1}\left(\frac{N_1-N_{1w}}{M_1+M_{1w}}\right) \tag{17}$$

in which M_{1w} and N_{1w} are the real and imaginary parts of the well location on the ζ_1-plane, respectively, and they can be obtained by letting $x = x_w$ and $y = y_w$ in equation (7).

Following the similar method and procedure as above, one can derive the solutions for S3–S5. For S3 (see Figures 2b1−2b3), after transformation, the solution of the complex potential (Ω_3) on the $\zeta_3=(\tau-1)^{1/2}=(\zeta_1^2-1)^{1/2}$-plane is similar to that of S1 with M_3 and N_3 expressed by:

$$M_3 = \Re[((M_1+iN_1)^2-1)^{1/2}] = \sqrt{\frac{\sqrt{((M_1^2-N_1^2-1))^2+(2M_1N_1)^2}+(M_1^2-N_1^2-1)}{2}} \tag{18}$$

$$N_3 = \Im[((M_1+iN_1)^2-1)^{1/2}] = \sqrt{\frac{\sqrt{((M_1^2-N_1^2-1))^2+(2M_1N_1)^2}-(M_1^2-N_1^2-1)}{2}} \tag{19}$$

in which $\Re$ and $\Im$ represent the real and imaginary parts of the function, respectively. Similarly, M_{3w} and N_{3w} are obtained by letting $M_1 = M_{1w}$ and $N_1 = N_{1w}$ in equations (18) and (19), respectively. For S4 (see Figures 2c1–2c3), after transformation, the complex potential (Ω_4) on the $\zeta_4=\tau^{1/2}$-plane can be derived by letting $\Phi_4^2=-\Phi_1^2$, $\Phi_4^4=-\Phi_1^4$, $\Psi_4^2=-\Psi_1^2$, and $\Psi_4^4=-\Psi_1^4$, respectively. Similarly, the complex potential of S5 (Ω_5) on the $\zeta_5=\tau^{1/2}$-plane can be obtained by letting $\Phi_5^2=-\Phi_1^2$, $\Phi_5^3=-\Phi_1^3$, $\Psi_5^2=-\Psi_1^2$, and $\Psi_5^3=-\Psi_1^3$, respectively (see Figures 2d1−2d3).

As mentioned above, the solution of S2 will be expressed in the series form. The complex potential of this scenario is first derived for the two infinite parallel constant-head boundaries, and then the effects of the image wells produced by two infinite parallel impermeable boundaries are superposed. The reason for this selection is explained in C. Lu et al., 2015, A note on the application of the image-well method for a rectangular boundary, submitted to Advances in Water Resources. The complex potential for a well between two constant-head boundaries is given by [*Intaraprasong and Zhan*, 2007, *Lu and Luo*, 2014]:

$$\Omega_2' = \frac{Q_w}{2\pi}\ln\left[\frac{\sin\left(\frac{\pi(z-z_w)}{2\lambda W}\right)}{\sin\left(\frac{\pi(z+\overline{z_w})}{2\lambda W}\right)}\right]+\Phi_0 \tag{20}$$

Superposing image wells generated from the two infinite parallel impermeable boundaries, the complex potential for S2 is expressed as:

$$\Omega_2 = \frac{Q_w}{2\pi}\sum_{n=-\infty}^{\infty}\ln\left[\frac{\sin\left(\frac{\pi(z-z_w-i2nW)}{2\lambda W}\right)}{\sin\left(\frac{\pi(z+\overline{z_w}-i2nW)}{2\lambda W}\right)}\frac{\sin\left(\frac{\pi(z-z_w-i(2n+1)W)}{2\lambda W}\right)}{\sin\left(\frac{\pi(z+\overline{z_w}-i(2n+1)W)}{2\lambda W}\right)}\right]+\Phi_0 \tag{21}$$

Separating Φ_2 and Ψ_2 from Ω_2 gives:

$$\Phi_2 = \frac{Q_w}{4\pi}\sum_{n=-\infty}^{\infty}\ln\left[\frac{(\cosh(\pi(y-y_w-2nW)/\lambda W)-\cos(\pi(x-x_w)/\lambda W))}{(\cosh(\pi(y-y_w-2nW)/\lambda W)-\cos(\pi(x+x_w)/\lambda W))}\right.$$
$$\left.\frac{(\cosh(\pi(y-y_w-(2n+1)W)/\lambda W)-\cos(\pi(x-x_w)/\lambda W))}{(\cosh(\pi(y-y_w-(2n+1)W)/\lambda W)-\cos(\pi(x+x_w)/\lambda W))}\right]+\Phi_0 \tag{22}$$

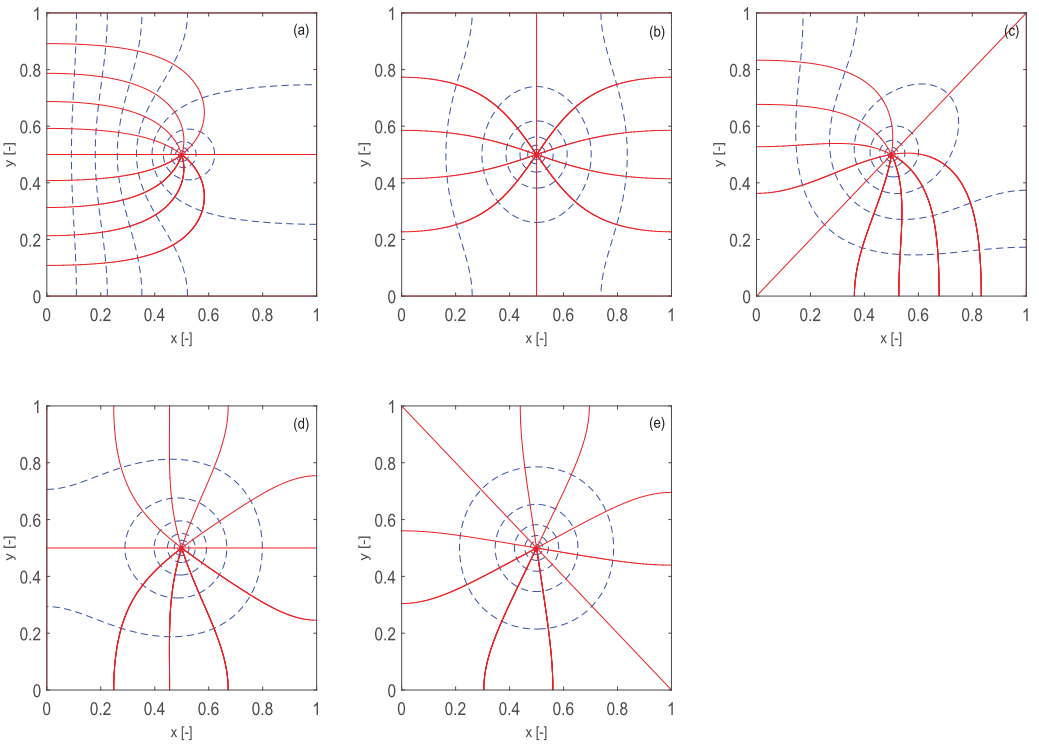

Figure 3. Constructed flow nets (streamlines in red and equipotentials in blue): (a) S1, (b) S2, (c) S3, (d) S4, and (e) S5.

$$\Psi_2 = \frac{Q_w}{2\pi}\sum_{n=-\infty}^{\infty}\left(\tan^{-1}\left[\frac{\sin(\pi x_w/\lambda W)\sinh(\pi(y-y_w-2nW)/\lambda W)}{\cos(\pi x_w/\lambda W)\cosh(\pi(y-y_w-2nW)/\lambda W)-\cos(\pi x/\lambda W)}\right]\right.$$
$$\left.+\tan^{-1}\left[\frac{\sin(\pi x_w/\lambda W)\sinh(\pi(y-y_w-(2n+1)W)/\lambda W)}{\cos(\pi x_w/\lambda W)\cosh(\pi(y-y_w-(2n+1)W)/\lambda W)-\cos(\pi x/\lambda W)}\right]\right) \quad (23)$$

Figure 3 shows the flow nets (streamlines and equipotentials) of S1–S5 based on the analytical solutions derived above, where $\lambda = 1$ and the sides of the square are normalized to 1. The significant discrepancy in these lines reflects the impact of different boundary condition combinations on the flow field.

3. Application

3.1. Problem Description

We consider a pumping well located in a confined flux-controlled coastal aquifer, as shown in Figure 4. It is assumed that the domain in plan view is rectangular, and bounded by the sea (constant-head), inland boundary (impermeable), and two lateral boundaries (impermeable). Therefore, the case corresponds to S1. Though the case assumed may not be physically realistic, it was employed in the study of *Mantoglou* [2003] and taken here as a demonstrative case.

We assume that the system is at the steady state condition and the interface between freshwater and seawater is sharp (i.e., the mixing between freshwater and seawater is neglected). In the absence of a well, a uniform regional flow with a constant rate of $q_f = 0.3\,\mathrm{m}^2/\mathrm{d}$ discharges to the sea over a stagnant seawater. The thickness between the confining later and the aquifer base is $B = 20\,\mathrm{m}$, and the hydraulic conductivity is $K = 10\,\mathrm{m/d}$. The domain length and width are $L[L]$ and $W[L]$, respectively. It is further assumed that the well is located at the center of the two lateral boundaries, and $x_w = 800\,\mathrm{m}$ from the coastline. For convenience, we assume that the coordinate system is the same as the one adopted above. As such, $y_w = W/2$.

3.2. Maximum Pumping Rate

Estimating the maximum possible pumping rate without pumping saltwater often interests water resources managers as well as well designers, since practical pumping rates below this critical value could keep the

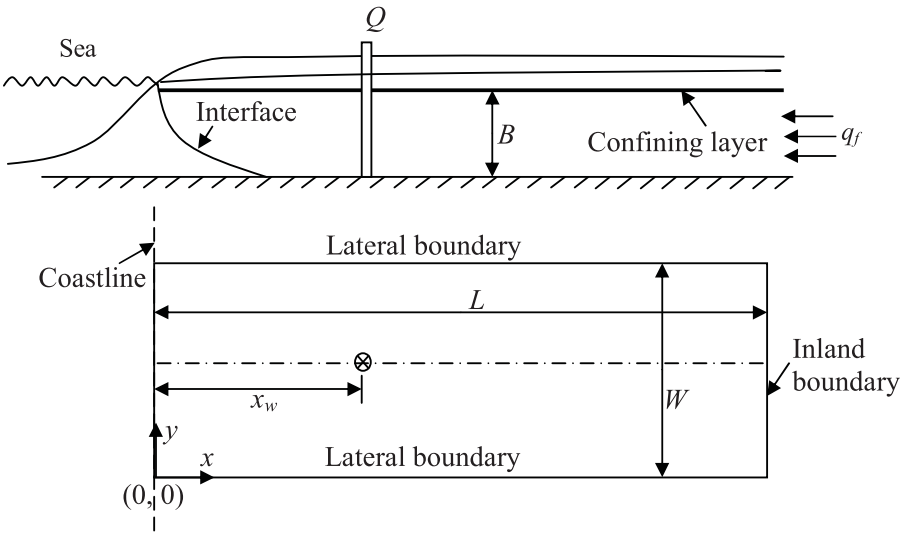

Figure 4. Conceptual model of a pumping well located in a fully bounded, flux-controlled, confined coastal aquifer: (a) cross section and (b) plan view.

production well sustainable. When a well extracts groundwater, there is a capture zone, within which groundwater can be extracted. Hence, the critical condition would occur when the stagnation point of the extraction well and the interface tip coincide [*Strack*, 1976]. Under such conditions, the interface is unstable as an infinitesimal increase of the extraction rate would cause saltwater upconing.

For the problem assumed above, three stagnation points can be found, with y_s being 0, $W/2$, and W. It is clear that $y_s=W/2$ is taken to derive the maximum pumping rate because the corresponding x_s of this stagnation point is the largest [*Lu and Luo*, 2014]. In other words, the stagnation point with $y_s=W/2$ is located most seaward, and hence critical to pumping saltwater. Therefore, a key step for determining the maximum pumping rate is to find the expression capable of deriving the x coordinate of the critical stagnation point. We exhibit the expression in Appendix B. With this expression, the maximum pumping rate Q_m can be determined by an iterative procedure, as explained in *Strack* [1976] and *Lu et al.* [2013].

3.3. Impact of Domain Size on Maximum Pumping Rate

Figure 5 shows the impact of W and L on Q_m, where W and L are varied between 1000 and 5000 m. As shown in Figure 5a, the domain size has a significant impact on Q_m, with the largest ($Q_m=403\,m^3/d$) and lowest ($Q_m=199\,m^3/d$) values obtained when $W=L=1000$ m and $W=L=5000$ m, respectively. Figure 5b

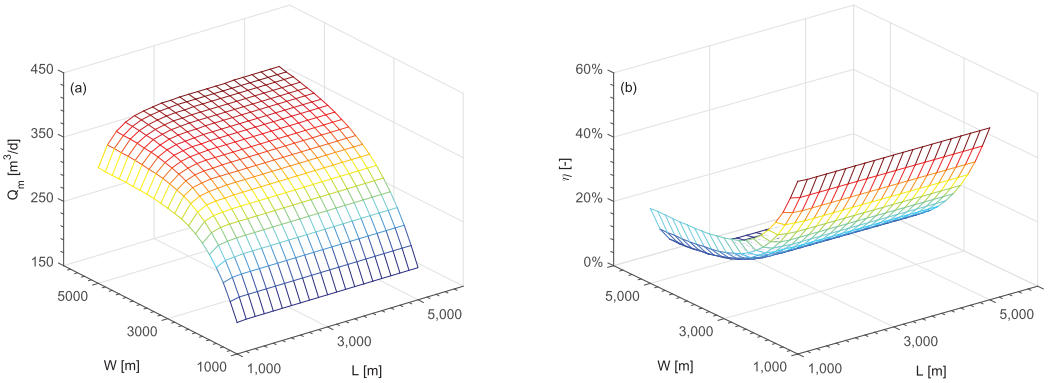

Figure 5. Impact of the domain size on the maximum pumping rate: (a) Q_m and (b) η.

shows the relative impact of the domain size on the maximum pumping rate, in comparison to a counterpart with $W=L=\infty$ (i.e., the scenario assumed in the study of *Strack* [1976]). The relative impact is quantified by $\eta=\frac{|Q_m-Q_m^s|}{Q_m^s}\times 100\%$, where Q_m^s is the *Strack*'s [1976] solution. The results indicate that when using numerical modeling to derive Q_m for cases with three impermeable boundaries at infinite distances, a significant error may occur if the domain size is not sufficient. For example, as $W=L=2000$ m, the relative impact from the domain size is about 27%. Hence, the analytical solution obtained can serve as a guide for designing the model domain size in numerical modeling, among other purposes.

4. Conclusion

Steady state analytical solutions for pumping in a rectangular aquifer with four different boundary condition scenarios have been developed using the Schwartz-Christoffel conformal mapping method together with the complex variable techniques. These four boundary condition scenarios share the same feature that the impermeable and constant-head boundaries can be combined after the conformal transformation. The developed analytical solutions are in the closed form, demonstrating the advantage of the conformal mapping method. By contrast, for the scenarios with two parallel impermeable boundaries and two parallel constant-head boundaries, the conformal mapping method fails since it is impossible to combine these two kinds of boundaries. As such, the solution must be expressed in the series form that superposes infinite image wells.

The developed analytical solutions can be applied to evaluate boundary effects in numerical simulations and laboratory experiments, and to assist in the management of coastal and noncoastal pumping wells. Note that the limitation of using the conformal mapping solutions lies in the range of the aspect ratio of the rectangle between 1/10.9 and 10.9/1. However, for aspect ratios out of this range the rectangle may be replaced by an infinite strip as the short boundaries will have minimal influence, except when the well is very close to one of them; the rectangle can then be replaced by a semiinfinite trip.

Appendix A: Proof of Equation (5)

The distance between points B (at $z=0$, $\zeta=0$) and C (at $z=\lambda W, \zeta=1$) in Figures 2a1 and 2b1 can be calculated by:

$$z_C-z_B=\lambda W=C_3\int_0^1\frac{d\zeta}{\sqrt{(1-\zeta^2)(1-m\zeta^2)}}=C_3K(m) \tag{A1}$$

Similarly, the distance between points B (at $z=0$, $\zeta=0$) and D (at $z=\lambda W+iW, \zeta=1\sqrt{m}$) can be calculated by:

$$z_D-z_B=\lambda W+iW=C_3\int_0^{1/\sqrt{m}}\frac{d\zeta}{\sqrt{(1-\zeta^2)(1-m\zeta^2)}}=C_3[K(m)+iK(1-m)] \tag{A2}$$

Combing equations (A1) and (A2) yields:

$$\frac{K(m)}{K(1-m)}=\lambda \tag{A3}$$

and

$$C_3=\frac{\lambda W}{K(m)} \tag{A4}$$

Appendix B: Derivation of the Location of the Stagnation Point

The x coordinates of the stagnation point are derived by setting the components of the discharge vector equal to zero. Since $y_s=W/2$ is known, we use $\frac{\partial\Phi}{\partial x}=0$ to derive x_s. The potential for the problem considered is expressed as:

$$\Phi=\Phi_1-q_f x \tag{B1}$$

The derivative of Φ with respect to x is given by:

$$\frac{\partial\Phi}{\partial x}=\frac{\partial\Phi_1^1}{\partial x}+\frac{\partial\Phi_1^2}{\partial x}+\frac{\partial\Phi_1^3}{\partial x}+\frac{\partial\Phi_1^4}{\partial x}-q_f \tag{B2}$$

in which $\frac{\partial\Phi_1^1}{\partial x}$, $\frac{\partial\Phi_1^2}{\partial x}$, $\frac{\partial\Phi_1^3}{\partial x}$, and $\frac{\partial\Phi_1^4}{\partial x}$ are expressed by:

$$\frac{\partial\Phi_1}{\partial x}=\frac{Q}{2\pi}\left[\frac{\frac{\partial M_1}{\partial x}(M_1-M_{1w})+\frac{\partial N_1}{\partial x}(N_1-N_{1w})}{(M_1-M_{1w})^2+(N_1-N_{1w})^2}\right] \tag{B3}$$

$$\frac{\partial\Phi_1^2}{\partial x}=\frac{Q}{2\pi}\left[\frac{\frac{\partial M_1}{\partial x}(M_1-M_{1w})+\frac{\partial N_1}{\partial x}(N_1+N_{1w})}{(M_1-M_{1w})^2+(N_1+N_{1w})^2}\right] \tag{B4}$$

$$\frac{\partial\Phi_1^3}{\partial x}=\frac{Q}{2\pi}\left[\frac{\frac{\partial M_1}{\partial x}(M_1+M_{1w})+\frac{\partial N_1}{\partial x}(N_1+N_{1w})}{(M_1+M_{1w})^2+(N_1+N_{1w})^2}\right] \tag{B5}$$

$$\frac{\partial\Phi_1^4}{\partial x}=\frac{Q}{2\pi}\left[\frac{\frac{\partial M_1}{\partial x}(M_1+M_{1w})+\frac{\partial N_1}{\partial x}(N_1-N_{1w})}{(M_1+M_{1w})^2+(N_1-N_{1w})^2}\right] \tag{B6}$$

where $\frac{\partial M_1}{\partial x}$ and $\frac{\partial N_1}{\partial x}$ are given as:

$$\frac{\partial M_1}{\partial x}=\frac{cn(x/C_3)dn(x/C_3)dn(y_s/C_3)}{C_3(cn^2(y_s/C_3)+msn^2(x/C_3)sn^2(y_s/C_3))}-\frac{2msn^2(x/C_3)cn(x/C_3)dn(x/C_3)sn^2(y_s/C_3)dn(y_s/C_3)}{C_3(cn^2(y_s/C_3)+msn^2(x/C_3)sn^2(y_s/C_3))^2} \tag{B7}$$

$$\frac{\partial N_1}{\partial x}=-\frac{sn(x/C_3)dn^2(x/C_3)sn(y_s/C_3)cn(y_s/C_3)}{C_3(cn^2(y_s/C_3)+msn^2(x/C_3)sn^2(y_s/C_3))}-\frac{mcn^2(x/C_3)sn(x/C_3)sn(y_s/C_3)cn(y_s/C_3)}{C_3(cn^2(y_s/C_3)+msn^2(x/C_3)sn^2(y_s/C_3))}-\frac{2msn(x/C_3)cn^2(x/C_3)dn^2(x/C_3)sn^3(y_s/C_3)cn(y_s/C_3)}{C_3(cn^2(y_s/C_3)+msn^2(x/C_3)sn^2(y_s/C_3))^2} \tag{B8}$$

Acknowledgments
The authors would like to thank Otto D.L. *Strack*, anonymous reviewers, and editors for their valuable comments and suggestions. The data used in this paper can be obtained upon request from the corresponding author.

References

Betz, A. (1948), *Konformal Abbildung*, 229 pp., Springer, Berlin.
Chan, Y. K. (1976), Improved image-well technique for aquifer analysis, *J. Hydrol.*, *29*, 149–164.
Corapcioglu, M. Y., O. Borekci, and A. Haridas (1983), Analytical solutions for rectangular aquifers with 3rd-kind (Cauchy) boundary conditions, *Water Resour. Res.*, *19*(2), 523–528.
Ferris, J. G., D. B. Knowles, R. H. Brown, and R. W. Stallman (1962), Theory of aquifer tests, *U.S. Geol. Surv. Water Supply Pap., 146–161, 1563-E.*
Howell, L. H., and L. N. Trefethen (1990), A modified Schwarz-Christoeffel transformation from elongated regions, *SIAM J. Stat. Comput.*, *11*, 928–949.
Intaraprasong, T., and H. Zhan (2007), Capture zone between two streams, *J. Hydrol.*, *338*, 297–307, doi:10.1016/j.jhydrol.2007.03.005.
Latinopoulos, P. (1982), Well recharge in idealized rectangular aquifers, *Adv. Water Resour.*, *5*, 233–235.
Lu, C., and J. Luo (2014), Groundwater pumping in head-controlled coastal systems: The role of lateral boundaries in quantifying the interface toe location and maximum pumping rate, *J. Hydrol.*, *512*, 147–156.
Lu, C., R. Gong, and J. Luo (2009), Analysis of stagnation points for a pumping well in recharge areas, *J. Hydrol.*, *373*, 442–452.
Lu, C., Y. Chen, and J. Luo (2012), Boundary condition effects on maximum groundwater withdrawal in coastal aquifers, *Ground Water*, *50*, 386–393, doi:10.1111/j.1745-6584.2011.00880.x.
Lu, C., A. D. Werner, C. T. Simmons, N. I. Robinson, and J. Luo (2013), Maximizing net extraction using an injection-extraction well pair in a coastal aquifer, *Ground Water*, *51*, 219–228.
Mantoglou, A. (2003), Pumping management of coastal aquifers using analytical models of saltwater intrusion, *Water Resour. Res.*, *39*(12), 1335, doi:10.1029/2002WR001891.
Strack, O. D. L. (1972), Some cases of interface flow towards drains, *J. Eng. Math.*, *6*(2), 175–191.
Strack, O. D. L. (1976), A single-potential solution for regional interface problems in coastal aquifers, *Water Resour. Res.*, *12*(6), 1165–1174.
Strack, O. D. L. (1989), *Groundwater Mechanics*, 732 pp., Prentice Hall, Englewood Cliffs, N. J.
Weber, S., and R. P. Chapuis (2013), Interpretation of a pumping test with interference from a neighboring well, *Ground Water*, *51*, 935–944.
Wilson, J. (1993), Induced infiltration in aquifers with ambient flow, *Water Resour. Res.*, *29*(10), 3503–3512.
Zhan, H. (1999), Analytical study of capture time to a horizontal well, *J. Hydrol.*, *217*, 46–54.